2 Experimental methods

2.1 Bulk magnetic characterisation

The magnetic characterisation of bulk materials was performed by employing standard magnetometers. These instruments allow the measurement of the magnetisation and the susceptibility of the samples. The susceptibility χ is a second rank tensor which is defined as:

$$\chi = \frac{\delta M}{\delta H} \qquad (2.1)$$

where M is the molar magnetisation of the sample and H is the magnetic field vector. Thus the susceptibility characterises the interaction of the magnetic moment of the samples with the external magnetic field. By looking at the molecular scale, the magnetic moment can be described as the energy variation of the molecular system (δE) due to the interaction with the magnetic field. The magnetic moment$m$ is defined as:

$$m = -\frac{\delta E}{\delta H} \qquad (2.2)$$

Considering a system characterised by an energy spectrum of n levels $E_n(n = 1,2,..,n)$ and introducing the Boltzmann distribution law, the macroscopic magnetisation can be written as:

$$M = \frac{N\sum_n(-\delta E_n/\delta H)exp(-E_n/kT)}{\sum_n exp(-E_n/kT)} \qquad (2.3)$$

where T is the temperature in K units and k is the Boltzmann constant. This is the general formula which directly relates the

energy levels description of the system to its macroscopic magnetic properties.

The measurement of magnetisation can be carried out by employing standard magnetometry techniques while for a correct evaluation of the susceptibility the use of alternating magnetic fields is required. These techniques are described in the following sections.

2.1.1 Standard magnetometry

Most magnetometers are based on the inductive detection. These instruments work with static magnetic field generated by a superconductive magnet. The magnetic flux variation induced by the presence of the sample inside a coil is measured. The flux variation produces in the coil an electromotive force proportional to $-\delta\phi/\delta t$ in the coil, where ϕ is the magnetic flux through the detection loops. In the coil circuit this generates a current that can be measured. To induce a time change of ϕ the magnetised sample is moved inside the detection coils in a region of homogenous magnetic field. During the measurements the sample is thus assembled on a rod and is moved inside a gradiometer circuit. This circuit is sensible only to a variation of the gradient of the magnetic field and allows to separate the contribution of the sample from the drift of the homogenous field. In particular, the second order gradiometer circuit employed in our instruments is formed by three coils, a single coil with N windings placed between two coils made of N/2 windings each and wound in the opposite direction (see fig. 2.1 left). The sample is moved from the centre of the top coil to the centre of the bottom coil. The current induced in the gradiometer circuit changes sign between opposite coils and the difference is assumed to be proportional to the magnetisation of the sample. The proportionality factor is determined through a calibration with standard samples with well-known magnetisation, like metallic Pt.

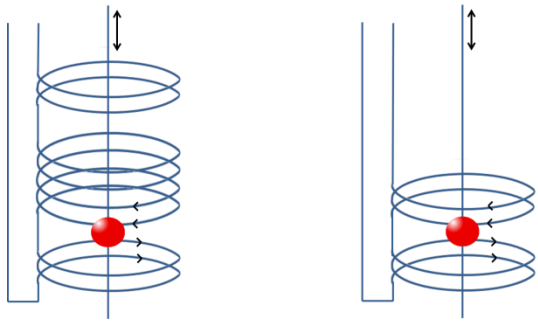

Fig. 2.1: Schematic representation of a second order gradiometer (left): the windings of the bottom and top coil are wound in the opposite direction respect to windings of the central one. In the magnetic measure the sample is moved up and down inside the gradiometer. A first order gradiometer made by two coils wound in the opposite way (right).

The sensitivity of the system can be enhanced by inductively coupling a Superconductive Quantum Interference Device (SQUID). This device, formed by a superconductive ring with a Josephson junction [1,2], is the most sensitive detector for the magnetic flux [3]. A comparable, although slightly lower, sensitivity can be reached employing a so called Vibrating Sample Magnetometer, VSM. In this type of magnetometers the sample is moved inside a gradiometer (fig. 2.1 right) at frequencies in the range of 50–100 Hz. The signal is recorded by means of a lock-in detection system without the necessity of a SQUID. This makes the magnetometer better suited for measurements under fast varying magnetic fields, which would be not compatible with SQUID devices, the latter being very sensitive to the magnetic field. The VSM technique was therefore used to record the magnetic hysteresis presented in section 3.2.

It is important to note that these magnetometers measure the magnetisation of the sample. The molar susceptibility χ can be calculated assuming a linear dependence of the magnetisation on the field as:

$$\chi = \frac{M}{N} \cdot H \qquad (2.4)$$

where M is the magnetisation of the sample and N is the number of moles. The assumption of a linear dependence of the magnetisation

on the field is not correct under strong magnetic fields. To have access to the susceptibility the so called *ac* susceptometry was employed.

2.1.2 Ac susceptometry

In these measurements the sample is positioned inside a coil, called primary. A small, few Oe, oscillating magnetic field can be generated by applying an alternate potential to the coil's ends. Inside the coil a first order gradiometer circuit is present, called secondary. Due to the opposite wounding of the two coils no voltage is induced from the primary to the secondary. However, if a sample is inserted in the coils it magnetisation will oscillates with the oscillating field unbalancing the secondary circuit, and generating a voltage that is proportional to the change in sample magnetisation. As the oscillating field is very small, the derivative of the magnetisation *vs.* the oscillating field, i.e. the susceptibility, is directly measured. The sample is moved inside the gradiometer to eliminate possible spurious signal due to a non-perfect balance of the gradiometer's windings.

It is possible to apply a constant field (B_0) along the same direction of the *ac* field. The total field experienced by the sample is thus:

$$B = B_0 + h\cos\omega t \qquad (2.5)$$

where h is the amplitude of the oscillation and ω is the angular frequency of the ac field. Independently from the value of B_0 the oscillating field remains small and thus the susceptibility can be evaluated also for a non-linear dependence of the magnetisation on the applied field.

The application of a tuneable *ac* field allows the study of the dynamic properties of the investigated sample by varying the angular frequency of the field. The magnetisation of the sample experiencing the *ac* field can be described as:

$$M(t) = M_0 + \chi(t)h \qquad (2.6)$$

It is convenient to describe the susceptibility as formed by a real, χ', and imaginary part, χ''. Thus $\chi(t)$ is:

$$\chi(t) = \chi' \cos\omega t + \chi'' \sin\omega t \qquad (2.7)$$

the magnetisation is then calculated as:

$$M(t) = M_0 + (\chi' \cos\omega t + \chi'' \sin\omega t)h \qquad (2.8)$$

The measurement of the two components can be achieved by using a lock-in detection. The relative value of the two components is determined by the dynamic properties of the investigated material in respect to the employed oscillation frequency. Defining τ as the time needed for a magnetic system to establish the thermal equilibrium in the oscillating field, two limiting cases can be encountered. If the frequency is slow comparing to the relaxation rate $\tau^{-1}(\omega\tau \ll 1)$ the magnetisation of the system is able to follow the oscillating field and no signal will be detected in the quadrature channel. The measured susceptibility is the isothermal one defined as χ_T. On the contrary when the frequency is fast comparing to τ^{-1} $(\omega\tau \gg 1)$ the susceptibility measured is the adiabatic susceptibility, χ_S. In this case the system has no time to exchange energy with surrounding environment. For intermediate ratios between omega and τ^{-1} Casimir and Du Pré [4] proposed the following formulae for the definition of the imaginary and real part of the susceptibility:

$$\chi' = \frac{\chi_T - \chi_S}{1+\omega^2\tau^2} + \chi_S \qquad (2.9)$$

$$\chi'' = \frac{(\chi_T - \chi_S)\omega\tau}{1+\omega^2\tau^2} \qquad (2.10)$$

For a system characterised by a distribution of relaxation times the two components of the susceptibility can be calculated as [5]:

$$\chi'(\omega) = \chi_S + (\chi_T - \chi_S)\frac{1+(\omega\tau)^{1-\alpha}\sin(\pi\alpha/2)}{1+2(\omega\tau)^{1-\alpha}\sin(\pi\alpha/2)+(\omega\tau)^{2-2\alpha}} \qquad (2.11)$$

$$\chi''(\omega) = (\chi_T - \chi_S)\frac{1+(\omega\tau)^{1-\alpha}\cos(\pi\alpha/2)}{1+2(\omega\tau)^{1-\alpha}\sin(\pi\alpha/2)+(\omega\tau)^{2-2\alpha}} \qquad (2.12)$$

where the phenomenological parameter α accounts for the distribution of relaxation times, the higher is α the wider is the distribution. By fitting the frequency dependence of the imaginary susceptibility with equation 2.12 the relaxation time τ and the α parameter can be evaluated. The procedure can also be repeated on χ', although this one does not show a peak feature. By repeating the measurements at different temperature it is possible to investigate the temperature dependence of the two parameters, τ and α. The same analysis can be repeated for different applied static fields. These studies are crucial for the investigation of the slow relaxation processes of SMM systems.

2.2 Sublimation process

One of the most clean techniques for the molecular deposition is the molecular sublimation in Ultra High Vacuum (UHV) environment (10^{-10} mbar). The UHV, indeed, allows to prepare clean surfaces by means of sputtering and annealing. Our home-made experimental setup for the sublimation process is illustrated in fig. 2.2. The powder of the molecular compound fills a quartz crucible housed in the turns of a tantalum wire. By means of Joule effect the crucible can be heated up controlling the temperature by a type K thermocouple immersed in the molecular powder. The heating process is controlled by regulating the current flowing in the tantalum wire by means of an adjustable power supply. The sublimation system is assembled on CF40 feedthrough and it can be assembled in UHV systems. The film preparation is thus achieved by heating up the powder to the

sublimation temperature while the sample surface is directly exposed to the incoming flux of molecules.

In order to exploit this process the molecules must be stable to thermal treatment. This is a quite restrictive prerequisite which, for example, limited the study of the Mn_{12} class of SMMs [6,7]. However, as anticipated in chapter 1, other SMMs are stable enough to be sublimated in UHV, as in the case of the $TbPc_2$ [8] and Fe_4Ph SMMs [9]. One of the most important advantages of the sublimation process, if compared to solution techniques, is certainly related to its cleanliness, which allows the best exploitation of scanning probe microscopy and related techniques. The possibility to deposit the same molecule on different substrates, including artificial structures not stable in ambient conditions, and the capability of controlling the amount of deposited molecules, are other relevant advantages of this UHV-based preparation technique. In particular in this work we exploited the versatility of the sublimation process to study $TbPc_2$ and Fe_4Ph SMMs on different substrates.

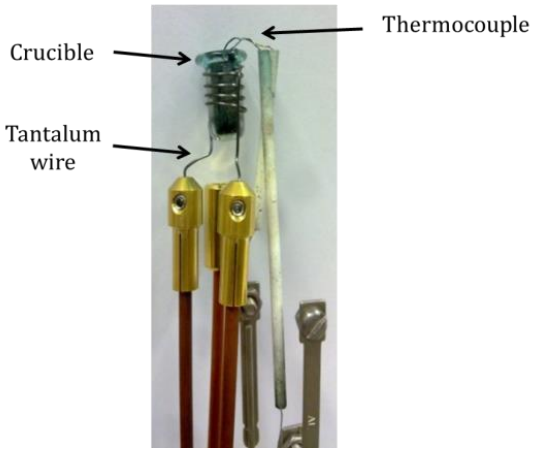

Fig. 2.2: A picture of the home built sublimating system.

2.3 Quartz Crystal Microbalance (QCM)

The quartz crystal microbalance is a useful tool for checking the molecular flux during the sublimation process. The sensor, made by a quartz crystal, detect small amounts of sublimated material on its surface by measuring the frequency variation of the crystal resonant oscillation. The relation between the mass of the deposited film and the frequency variation is:

$$\Delta s = \frac{K}{\rho \cdot z \cdot f_c} \tan^{-1}\left\{ z \tan\left[\frac{\pi(f_q - f_c)}{f_q}\right]\right\} \qquad (2.13)$$

where Δs and ρ are the thickness and the density of the deposited material respectively, f_c and f_q are the frequency before and after the deposition, respectively, and K is a constant including quartz crystal parameters; z is the so called z-factor which is tabulated for many materials, in our experiments we used the value of the graphite.

2.4 Photoelectron Spectroscopy (PES)

The chemical characterisation of the sublimated films on conductive substrates can be performed by employing the photoemission technique (PES). The technique is based on the photoemission effect, which was discovered by H. Hertz in the 1887. The effect was then rationalized in the following years by Einstein (1905) [10] and its application in spectroscopic studies was developed only in the '50s and '60s. The technique was refined during the last 60 years to achieve the actual state of the art.

The photoemission effect takes place when a photon transfers enough energy to an electron to overcome the potential barrier (binding energy) holding it to its atom. The exceeding energy imparted by the photon manifests as kinetic energy of the electron.

Thus knowing the photon energy ($h\upsilon$) and the kinetic energy (E_{Kin}) of the photoelectron it's possible to calculate the binding energy (E_B) using the following formula:

$$E_B = h\upsilon - E_{Kin} + \phi_{samp.} - \phi_{spec.} \qquad (2.14)$$

where $\phi_{samp.}$ and $\phi_{spec.}$ are the work functions of the sample and spectrometer (fig. 2.3). The energy level diagram of the process is depicted in fig. 2.3 considering the case of a metallic sample electrically connected to the spectrometer and both grounded. This allows for minimising the charging effect maintaining a fixed potential during the photoemission process.

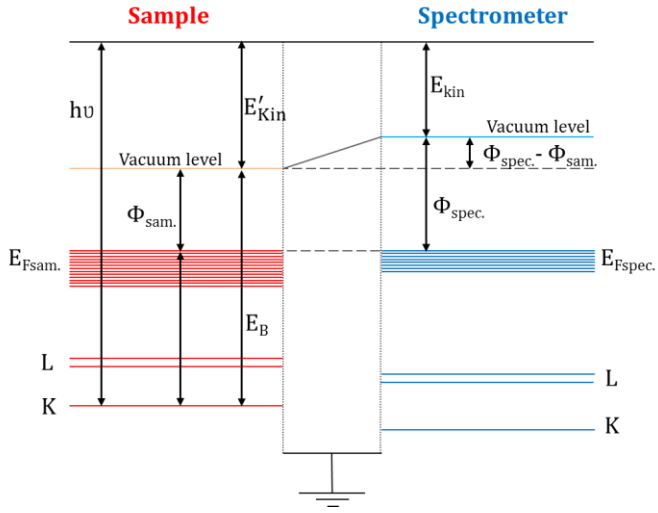

Fig. 2.3: Sample levels scheme (red) and spectrometer levels (blu). The sample and the spectrometer are in direct contact, thus their Fermi energies are equal. When photoelectrons go from the sample to the spectrometer they feel a potential due to the difference of the workfunctions of the two materials.

The scheme considers a system at 0 K where the Fermi level is the highest occupied energy level. At the equilibrium the sample and the spectrometer have the same Fermi energy due to the electrical contact. When the photoelectron goes from the sample into the spectrometer it feels an accelerating or decelerating potential due to the difference in work function of the two materials ($\phi_{samp.} - \phi_{spec.}$).

The work function is defined as the energy difference between the Fermi and the vacuum level and it depends on the material. Although the Fermi levels of the sample and spectrometer are the same they have different work functions. This introduces a shift in the detected kinetic energy of the electrons that must be corrected to be able to compare spectra acquired with different spectrometers.

The PES spectrum is acquired recording the number of electrons detected in function of their kinetic energy. However, since the kinetic energy depends on the radiation energy, the use of the binding energy abscissa is generally preferred. It's important to note that in PES experiments the energy level of the final state is measured, which is lacking one electron, while energy of the initial state can be only obtained by theoretic considerations.

In some cases the photoemission process involves also a transition of a core electron into the valence band. In this case the final ionised atom is not in its ground state, and the kinetic energy E'_{Kin} of photon resulting from this two electrons process is lower than the expected one (fig. 2.4) and also depends on the energy of the excited state.

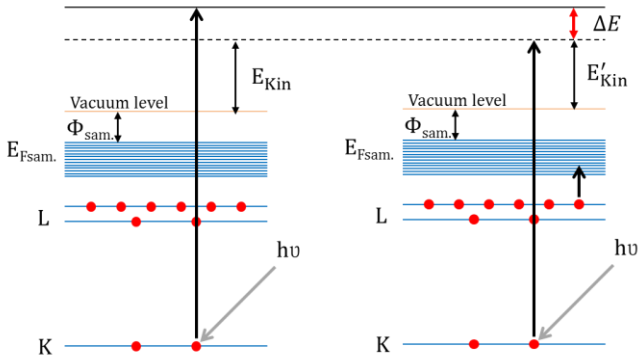

Fig. 2.4: Scheme of the levels in the description of the shake-up satellite peaks generation; the one electron process(left) and the two electron process (right).

It can be calculated as respect to the E_{Kin} of the one electron process as:

$$E'_{Kin} = E_{Kin} - \Delta E \qquad (2.15)$$

which corresponds in binding energy:

$$E'_B = E_B + \Delta E \qquad (2.16)$$

where ΔE is the energy involved in the transition of the core electron to the valence band. This process leads to discrete structures at higher binding energy side of the main photoelectron peak (shake-up satellite(s)).

Strong satellite peaks are generally observed in many transition metal and rare earth based compounds. In particular in the XPS spectrum of compounds containing Fe^{3+}ions show strong shake-up satellites (see sections 4.2 and 4.3) and this is an additional feature that can be used to recognise it. Moreover emitted photoelectrons can leave the sample's surface directly or they can interact with the atoms of the sample before escaping from the surface. The *primary spectrum* is formed by photoelectrons which leave the surface without exchanging energy with the surrounding atoms. The *secondary spectrum* is formed by the photoelectrons which have exchanged energy by means of inelastic scattering processes and it contributes to form a background. The latter ones are labelled as *secondary electrons* and their energy cannot be calculated with equation 2.14.The scattering processes limit the escape length of the emitted photoelectrons giving rise to one of the more interesting properties of the photoelectron spectroscopy. Photoelectrons with energy >50 eV allow to investigate a thickness of a maximum 50 Å.This feature makes the technique surface sensitive. The short escape length is also the reason for the necessity to work in ultra-high vacuum conditions. The surface sensitivity of the PES technique requires an atomically clean surface. Thus 10^{-10} mbar base pressure is recommended for PES investigations. A schematic representation of the PES experiment is reported in fig. 2.5.

According to the radiation energy used the photoelectron spectroscopies are classified as X-ray Photoemission Spectroscopy (XPS) and Ultraviolet Photoemission Spectroscopy (UPS).

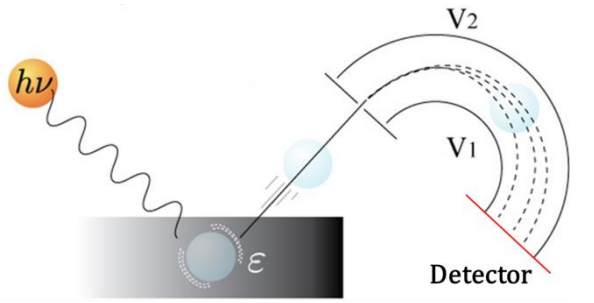

Fig. 2.5: The X-ray photon (hυ) excites the electrons of the sample which are emitted as photoelectrons. The photoelectrons are then separated in energy by means of a hemispherical analyser.

2.4.1 X-ray Photoemission Spectroscopy (XPS)

In a XPS experiment the incident photons have energies $100 < h\nu < 1500$ eV; the most common X-ray sources used in a conventional laboratory are the Al Kα (1486.6 eV) and Mg Kα (1253.6 eV). The photon energy is thus enough to promote core electrons into the vacuum continuous level of the investigated samples. As already mentioned the binding energy of the photoelectrons can be used as fingerprint of the element allowing a chemical analysis of the surface. Each peak is labelled with the corresponding level of the initial state. The photoemission peak associated with an electron ejected from an orbital characterised by $l > 0$ can show a well-defined splitting in two components. The two states derive from the spin-orbit coupling. Accounting for the spin-orbit coupling with the j-j coupling scheme the total angular momentum of each electron is given by $j = l + s$ and the total angular momentum of the whole atom is calculated as $J = \sum j$. Two possible states arise when an electron is ejected from an orbital characterised by $l > 0$. The difference in energy of the two states is due to the parallel or antiparallel alignment of the spin electron and its orbital angular momentum i.e. $j = l \pm \frac{1}{2}$. This separation for the core shells can be many electron-volts and is another fingerprint of a specific element. The relative intensity of the peaks is given by the

ratio of their respective degeneracies $(2j + 1)$. An example of the spin-orbit splitting is reported in fig. 2.6 for the Au *4f* peak.

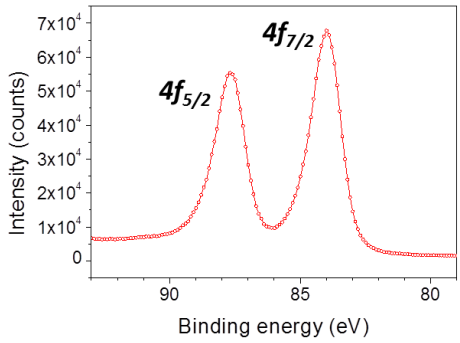

Fig. 2.6: Spin splitting of the Au *4f* region: the two components $4f_{5/2}$ and $4f_{7/2}$ are separated by 3.67 eV.

The binding energy of the peaks depends also on the electronic density of each atom that is related to the chemical environment, i.e. oxidation state and functional groups present (*chemical shift*). For instance the Fe^{3+}, Fe^{2+} and Fe^{0} *2p* peaks have not the same binding energy: the core electrons of atoms with low electron density (like Fe^{3+}) feel stronger Coulomb interaction respect to a more reduced species (like Fe^{2+}), therefore the energy required for the ionisation process is shifted to higher values. This phenomenon allows for discriminating the oxidation state of each element on the surface.

In order to compare the intensity of different XPS peaks the relative atomic photoemission cross-section (σ) must be taken into account. This parameter depends on the atomic initial state and on the photon energy. A complete table of the element photoemission cross-section can be obtained from the web address: http://ulisse.elettra.trieste.it/services/elements/WebElements.html. [11,12]. The tabulated values have been used in this work for the quantitative interpretation of the XPS spectra. The intensity of each peak can be evaluated by integrating the corresponding area after the subtraction of the inelastic background. This process can be performed by using one of the many available programs which allow the deconvolution of the XPS signal and the background subtraction.

The calculated area is then divided by its relative cross section allowing the comparison between the intensity of the peaks of different elements. In this way it is possible to estimate the surface chemical composition with a typical accuracy of 10 %.

The XPS technique is also a useful tool for the estimation of the film thickness. By assuming the system as constituted by a uniform deposit, A, on the substrate surface, B, (fig. 2.7), and considering the escape length of the photoelectron emitted from the film equal to the escape length of photoelectrons emitted from the substrate, we obtain the following simplified equation:

$$\frac{I'_A}{I'_B} = \frac{N_A\left\{1-exp\left[-d/\lambda_{A,A}cos\theta\right]\right\}}{N_B\left\{exp\left[-d/\lambda_{B,A}cos\theta\right]\right\}} \qquad (2.17)$$

Where $\lambda_{A,A}$ and $\lambda_{B,A}$ are the inelastic mean free paths of the electrons in A (second index letter) emitted by the element A or B (first index letter), and N_A and N_B are the number of atoms constituting the investigated surface portion. The emission angle θ of the electrons is given with respect to the surface normal (polar angle). If the A and B peaks are close in energy is possible to approximate $\lambda_{A,A} \sim \lambda_{B,A} = \lambda$ and write for the layer thickness d:

$$d = \lambda cos\theta \ln\left(\frac{I'_A N_B}{I'_B N_A} + 1\right) = \lambda cos\theta \ln\left(\frac{I'_A I_{B\infty}}{I'_B I_{A\infty}} + 1\right) \qquad (2.18)$$

where $I_{A\infty}$ and $I_{B\infty}$ are the intensities of the signals of pure bulk elements A and B. The accuracy in the estimation of d using this equation is affected by the incertitude on N_B/N_A and $I_{B\infty}/I_{A\infty}$. With a good approximation we can assume that $I_{B\infty}$ and $I_{A\infty}$ are equal to the photoionisation cross section of the respective element, while I'_A and I'_B correspond to the intensity of XPS signal. In this case all the parameter of the equation 2.18 are known allowing the calculation of d thickness. If the $\lambda_{A,A} \sim \lambda_{B,A} = \lambda$ approximation is not reasonable the equation can be solved numerically introducing the escape length calculated for each element.

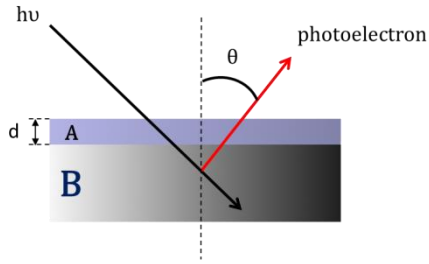

Fig. 2.7: Schematic representation of a uniform film deposit (A) on top of the substrate (B).

2.4.1.1 Auger emission

In this discussion we have considered only the process involving photoelectrons. However when the X-ray radiation interacts with the atoms of the surface another process can produce electron emission. This is the case of the Auger process. For the clarity of the discussion we can consider the ionisation of the K shell by means of the photon interaction. The vacancy created in the K shell can be filled by an electron of the L shell with the release of energy in a radiative way, i.e. emitting a photon, or by emitting a second electron: the Auger electron (fig. 2.8). The Auger transition is indicated with the historical X-ray notation; states with n=1,2,3,4... are labelled as K,L,M,N... respectively, while states with various combination of l=0,1,2,3,4...and j=$\frac{1}{2},\frac{3}{2},\frac{5}{2},\frac{7}{2}$, ... are given conventional suffixes 1,2,3,4... For example the $2p_{3/2}$ spectroscopic level is labelled in the historical X-ray notation as L_2 ($2p_{1/2}\rightarrow L_3$; $3d_{5/2}\rightarrow M_5$; $3d_{3/2}\rightarrow M_4$). This notation will be used in the XAS experiments reported in section 3.4. The $KL_1L_{2,3}$ Auger emission corresponds to the decay of an electron from the level *2s* (L_1) to the level *1s* (K) with emission of an electron from the level $2p_{1/2,3/2}$ ($L_{2,3}$). The energy of the emitted Auger electrons is not correlated to the X-ray excitation energy and it depends only on the energy levels of the system. In some cases the emitted Auger electrons of an element present on the surface sample have the same energy of the XPS peak of another element. This phenomenon, as in

the case presented in sections 4.5 and 4.6, can sometime hamper a correct estimation of the XPS signals.

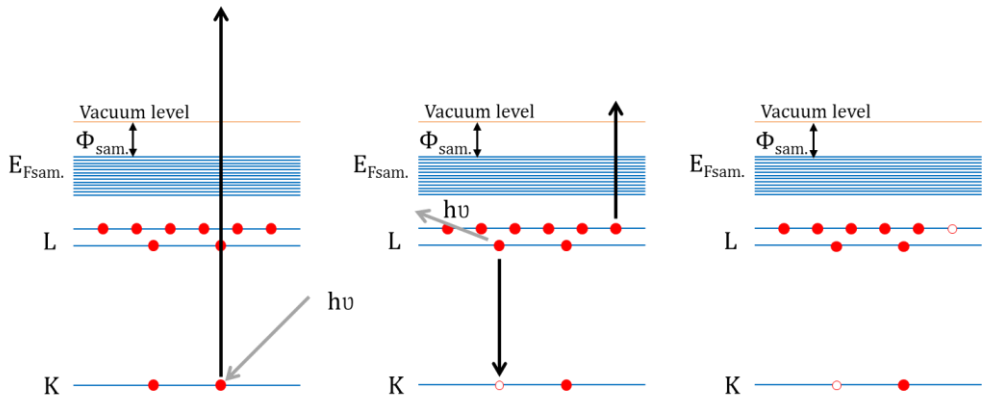

Fig. 2.8: Schematic representation of the Auger emission process. The photon excites a core electron of the K shell (left) the hole is filled by an electron of the L shell. The energy involved can be emitted as photon or can give up to the Auger electron (centre). The final state is a double ionised atom (right).

2.4.2 Ultraviolet Photoemission Spectroscopy (UPS)

In the UPS technique the incident photons have energies $10 < h\nu < 50$ which are enough to remove the electrons from the valence band. The most common laboratory source for ultraviolet photoemission spectroscopy is the helium discharge lamp, which can provide photons with energy of 21.2 eV He(I) and 40.8 eV He(II). UPS, allowing the study of the valence band, provides useful information about the electronic structure of the surface and of molecular films. By comparison of the UPS spectrum with the calculated density of state (DOS) of the isolated molecule it is possible to evaluate the intactness of the molecules and their interaction with the substrate. An example of UPS spectrum acquired on the clean Au(111) surface is reported in fig. 2.9.

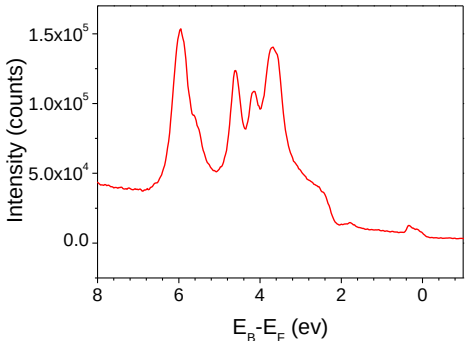

Fig. 2.9: UPS spectrum of the Au(111) valence band; the zero of the energy scale is set to the Fermi energy of the gold.

2.5 X-ray Absorption Spectroscopy (XAS)

The synchrotron based X-ray absorption spectroscopy is a fundamental tool for the magnetic and structural investigation of thin films [13]. In fact, the magnetic characterisation of monolayer and submonolayer molecular films cannot be carried out using the standard magnetometry techniques because these are not able to measure the signal of such small amounts of magnetic materials [14].

The fundamental properties of XAS can be summarized as follow:

- *Element specificity*. The X-ray absorption involves the electronic level of the atoms, thus the energy of the transitions is a fingerprint of the specific element.

- *Sensitivity to electronic state (or valence).* The feature and the energy of the peaks are related to the oxidation states of the investigated atomic species.

- *Sensitivity to the spin.* By using circular polarised X-ray light and measuring the dichroism (XMCD) it is possible to investigate the magnetism of the absorber.

- *Sensitivity to the anisotropy of the charge distribution around the absorbing atom.* By using linearly polarised light it is possible to measure the X-ray Natural Linear Dichroism (XNLD) which is indicative of the orientation of the different molecular orbitals that can be due to a preferential orientation of the molecules.

- *Surface sensitivity*. Using the appropriate detection mode the technique is sensitive only to the top-most atomic/molecular layers of the surface.

X-ray absorption and the related dichroism can be measured only using X-ray synchrotron sources. In third generation synchrotron it is possible to produce polarised X-ray light tuneable in energy with a large flux of photons.

2.5.1 X-ray synchrotron radiation

The synchrotron radiation is generated by deviation of an accelerated electron beam by means of magnetic fields. This process gives rise to the emission of a wide and continuous electromagnetic spectrum. The electron beam is generated by thermionic emission process by means of an electron gun in UHV environment. The electrons are collimated and accelerated to hundreds MeV energy before being introduced in a booster ring where their energy is further increased to reach the final energy of few GeV. The electrons are then introduced in the storage ring, where theirs linear trajectory is deviated by means of magnetic fields (quadrupole units). In the linear sections of the storage ring additional devices are inserted "disturbing" the pathway of electrons, this process leads to the emission of electromagnetic radiation along the tangent to the electrons trajectory. Photons produced are collected and used for experiments in several beamlines built along the ring.

The main properties of the radiation of each beamline are due to the used system for the photon emission. In particular for the

beamline working on XAS-derived techniques the so called "insertion device", which is made by periodic arrays of magnets placed above and below the electron pathway (fig. 2.10), is employed. The insertion devices are divided in two classes the *wigglers* and the *undulators*. The main differences are related to the range of photon energies emitted and the collimation of the light. The *wigglers* produce low collimated high energy photon (10-20 KeV) spread on a wide range of energies. The *undulators* generate high collimated energy photon with a narrow spectral emission range. The maximum of the spectral emission can be tuned by changing the distance of the two rows of magnets above and below the electrons path (fig. 2.10). In both *insertion devices* the emitted photons are linearly polarised. However by using two or more set of *undulators* it is possible to possible to obtain also the circularly polarised light needed for the XMCD measurements.

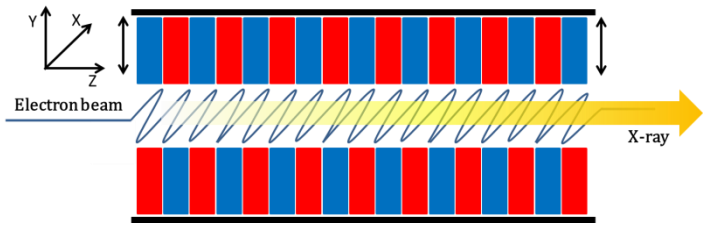

Fig. 2.10: Schematic representation of an insertion device. The red and blue elements are permanent magnets aligned in two rows, one above and one below the electron beam. In the *undulator* the gap distance between the two rows can be modified to tune the spectral emission.

2.5.2 X-ray absorption spectroscopy principles

The simplest way to describe X-ray absorption process is the so called *one electron approximation* [15]. In this description the photon transfers its energy to a single core electron which is promoted from the core level to the valence band neglecting all the other electrons in the process. This view is clearly an oversimplification of the physics involved in the process and it does not allow a quantitative

interpretation of the spectra. A more correct way to describe the phenomenon is the *configuration picture.* In this interpretation an atom is excited from its initial to the final excited configuration. Both configurations are described by theirs total angular momentum (J) which can be calculated with the (j-j) coupling scheme, as described in section 2.5.1, or by the so called Russell-Saunders (RS) coupling:

$$L = \sum l_i \qquad S = \sum s_i \qquad J = L + S$$

where L and S are the total angular orbital momentum and the total spin angular momentum respectively, the l_i and s_i are the angular and spin momentum of the single electrons, respectively. This description allows to take in account the angular momentum interaction between the excited electron and the other electrons belonging to the same atom.

The cross-section of the X-ray absorption process is calculated considering a time dependent perturbation to the electronic levels induced by the electromagnetic field. The transition probability from the initial state $|i\rangle$ to the final state $|f\rangle$ functions (both containing an electronic and a photon part) can thus be described following the formalism developed by Kramers [16] and by Dirac [17] as:

$$T_{if} = \frac{2\pi}{\hbar}\left|\langle f|H_{int}|i\rangle + \sum_n \frac{\langle f|H_{int}|n\rangle\langle n|H_{int}|i\rangle}{\varepsilon_i - \varepsilon_n}\right|^2 \rho(\varepsilon_f) d(\varepsilon_i - \varepsilon_f) \qquad (2.19)$$

where ε_i, ε_f are the energy of the initial and the final state respectively, $\rho(\varepsilon_f)$ is the density of the final state per unit of energy and $H_{int} = \frac{e}{m_e}\vec{p}\cdot\vec{A}$ is the Hamiltonian describing the interaction with the electromagnetic field. Where e, m_e and $\vec{p}$ are the charge, the rest mass and the moment of the electron respectively and $\vec{A}$ is the potential vector. Just for clarity of the discussion we report that the electric field can be obtained as $\vec{E} = -\frac{\overrightarrow{\delta A}}{\delta t}$. The cross-section (σ) is thus obtained from the transition probability by normalizing for the total incident flux (ϕ_0):

$$\sigma = \frac{T_{if}}{\phi_0} \qquad (2.20)$$

2.5.3 X-ray Magnetic Circular Dichroism (XMCD)

The X-ray Circular Dichroism (XMCD) technique allows the characterisation of the magnetic properties of the inspected material. In particular it provides information about the intensity and the direction of the magnetic moment of the probed element. It's important to recall the properties of the XAS experiment which allows element selectivity. The XMCD is thus able to measure magnetic moments of different elements present in the same sample.

In order to explain the basis of the XMCD experiment is convenient to refer to the *2p* → *3d* transition of transition metals (fig. 2.11). In this case the small orbital moment of the *d* shell is quenched by the crystal field and the shell has only the spin moment. In order to be able to measure the difference in the spin state of the *d* shell we need to made the XAS process spin dependent. By using circular polarisation is possible to selectively excite the spin-up or spin-down photoelectron from the core shell. Since the XAS does not allow spin flip processes the photoelectron spin-up (spin-down) can be only excited in spin-up (spin-down) final states. The intensity of the transition thus reflects the density of the empty final states for the spin-up and spin-down respectively. In fact, if the electron is excited from a spin-orbit split level the photon can transfer part of its angular momentum to the electron trough the spin-orbit coupling. The left circular polarised light transfers opposite angular momentum of the right one. In the transition *2p* → *3d* the spin-orbit coupling split the *2p* state in the $2p_{3/2}$ (L_3edge) and $2p_{1/2}$ (L_2 edge) states with opposite alignment of the two components. The spin polarisation of the photoelectron is the opposite in the two cases. The magnetic information is related to the spin-split valence band which acts as a detector for the photoelectrons and, as already mentioned, the intensity of the absorption is proportional to the density of the empty *d* final states. If the *d* valence band possesses an orbital momentum it

can also act as orbital momentum detector allowing to separate the spin and orbital contribution to the magnetic moment. The quantification of the two contributions can be account by using the *sum rules* (see section 2.5.3.1).

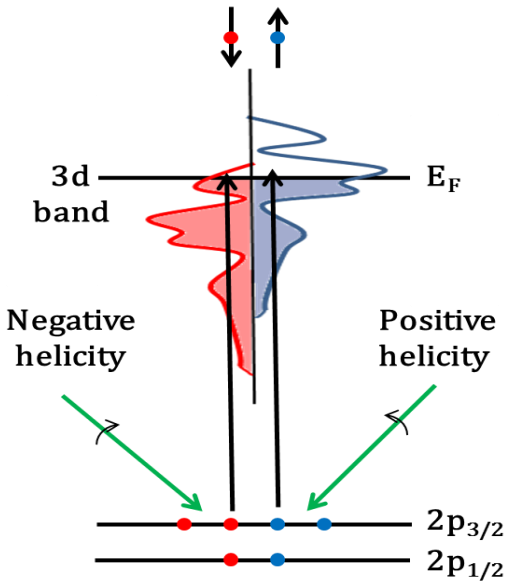

Fig. 2.11: Schematic representation of the circular polarised light absorption. The different probability of the two transitions gives rise to the XMCD signal at the L_3 edge.

The XAS spectra of a Co film acquired with the two circular polarisations and the resulting XMCD spectrum are reported in fig. 2.12. Considering the left circular polarisation (σ^+ the relative cross-section) with the helicity pointing to the photon propagation direction and considering the reverse for the right polarisation (σ^- the relative cross-section) the XMCD spectrum is defined as:

$$XMCD = \sigma^- - \sigma^+ \qquad (2.21)$$

The size of the dichroism effect scales like $cos\Theta$, where Θ is the angle between the photon spin and the magnetisation direction. Thus the maximum dichroism is revealed when the helicity of the photon lays in the same direction (parallel or anti-parallel) of the quantization axis of the *d* shell, i.e. in the magnetisation direction.

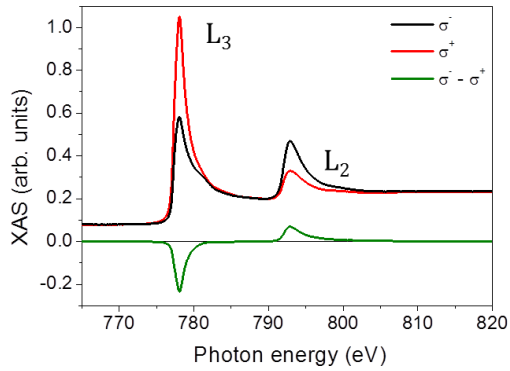

Fig. 2.12: XAS absorption spectra acquired with left ($\boldsymbol{\sigma^+}$) and right ($\boldsymbol{\sigma^-}$) circular polarisation of a thin film of cobalt evaporated on Cu(100) and the relative XMCD spectrum ($\boldsymbol{\sigma^- - \sigma^+}$).

2.5.3.1 Sum rules 2p → 3d

The sum rules were reported by Thole et al. [18] and Carra et al. [19], allowing the determination of the orbital and spin moments. A complete discussion about the details of the calculation is beyond the aim of this work. Here only the general results which allow the calculation for the *2p → 3d* ($L_{2,3}$edges) are presented. For such transitions the angular momentum (m_{orb}) can be calculated as:

$$m_{orb} = -\frac{4\int_{L_2+L_3}(\sigma^- - \sigma^+)d\omega}{3\int_{L_2+L_3}(\sigma^+ + \sigma^-)d\omega} \cdot (n_{3d}) \qquad (2.22)$$

where m_{orb} is in units of μ_B/atom, $(\sigma^- - \sigma^+)$ is the XMCD spectrum, and n_{3d} is the number of the *3d* holes of the specific transition metal atom. Similar formula allows the calculation of the spin momentum (m_{spin}):

$$m_{spin} = \frac{6\int_{L_3}(\sigma^- - \sigma^+)d\omega - 4\int_{L_2+L_3}(\sigma^- - \sigma^+)d\omega}{\int_{L_2+L_3}(\sigma^+ + \sigma^-)d\omega} \cdot (n_{3d}) \cdot \left(1 + \frac{7\langle T_z\rangle}{2\langle S_z\rangle}\right)^{-1} \qquad (2.23)$$

where the $\langle T_z \rangle$ is the expectation value of the magnetic dipole operator and $\langle S_z \rangle$ is equal to half of the m_{spin} in Hartree atomic units. By neglecting the $\frac{\langle T_z \rangle}{\langle S_z \rangle}$ ratio contribution [20,21] it is possible to calculate the two contributions from the direct integration of the XAS and XMCD spectra. The integral $\int_{L_2+L_3}(\sigma^+ + \sigma^-)d\omega$ can be evaluated after the subtraction of a two step background function with (L_3:L_2 ratio 2:1 in agreement with their 2j+ 1 degeneracy).

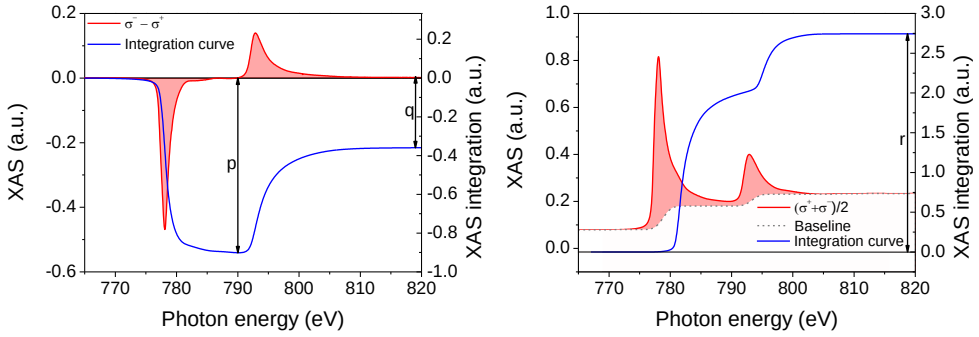

Fig. 2.13: Integration of the cobalt XMCD spectrum (left) and the integration of the XAS spectrum calculated as $(\boldsymbol{\sigma^- + \sigma^+})/\mathbf{2}$ after the subtraction of the two steps background.

Referring to fig. 2.13 the orbital and spin momenta can be thus calculated as [20]:

$$m_{orb} = \frac{-4q \cdot n_{3d}}{2r} \qquad (2.24)$$

$$m_{spin} = \frac{-(6p-4q) \cdot n_{3d}}{6r} \qquad (2.25)$$

2.5.4 X-ray Natural Linear Dichroism (XNLD)

The XNLD experiment is defined as the difference between the XAS spectra acquired with vertical and horizontal polarised light. The

XNLD technique provides information about the anisotropy of the charge distribution around the absorbing atom. This information can be useful for individuating preferential orientation in SMM hybrid surfaces [14]. A simple way to visualize the phenomenon originating the linear dichroism is to invoke the so called "search light effect" introduced by Stöhr *"X-ray absorption is governed by electric dipole transition and the photoelectrons are preferentially excited into the direction of the electric field"* [22]. The dichroism derives from the anisotropy in the valence level of the investigated atom. Considering a transition *2p* → *3d* its intensity is related to the sum over all the degenerate *2p* states and all the *3d* states. The core levels leads to a spherical symmetry contribution. The *3d* orbital contribution is strictly related, in mononuclear molecular complexes, to the symmetry of the complex. In cubic symmetry the *3d* degeneracy is broken by the ligand field obtaining the t_{2g} and e_g irreducible representations. The sum of each representation gives rise to a spherical contribution. In this situation no dependence on the photon electrical field orientation has to be expected. However lowering the symmetry of the complex the contribution is no more spherically symmetric and a dependence on the electrical field orientation is found. The intensity of the transition is then at its maximum when the electric field points to the empty states and it will be zero on nodal plane. This allows to extract information about the local symmetry of the absorber.

2.5.5 X-ray absorption detection

As reported in the previous chapters the XAS absorption leads to a core hole final state. This state is not stable and it evolves relaxing in two principal ways: by the emission of Auger electrons or by emission of fluorescence photons. Both emissions are related to the probability of the XAS absorption and thus they can be measured in function of the photon energy to provide the XAS spectrum. Different detection methods can be employed for the two emissions. In this

work the Total Electron Yield (TEY) mode was used. The Auger emission leads to ionised atoms. If the sample is grounded an electron current flows to the sample to restore the neutrality. This current can be read by means of a picoammeter (fig. 2.14). Since the process is related to the emission of the Auger electron the TEY mode is surface sensitive. In fact the escape length of the Auger electrons is ~2 nm and no information on processes occurring deeper in the sample is accessible. This detection method allows the study of the superficial properties of the samples.

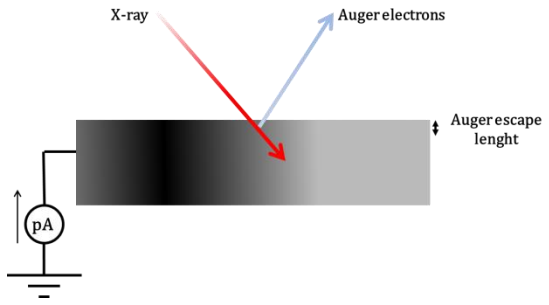

Fig. 2.14: Schematic representation of the total electron yield (TEY) detection system.

2.6 DEIMOS beamline

Most XAS experiments carried out during this thesis work have been performed on the DEIMOS beamline, which will be shortly described here. DEIMOS beamline experimental setup was designed to perform XAS and its derivate techniques. The beamline's photon energy range is 250-2500 eV. The *insertion device* allows the study with linearly and circular polarised light. A cryo-magnet allows measuring the XAS at temperature as low as 1.5 K with tuneable magnetic field along the photon direction up to 70 kOe.

Two preparation chambers connected to the beamline allows the *in situ* preparation of the sample (fig. 2.15). In particular the MBE chamber was dedicated to the surface preparation and provides

sputtering/annealing and metal evaporation facilities. The other (RAOUL) was employed for the molecular sublimation. The UHV system offers also the possibility to characterise the investigated surfaces by STM, LEES, and Auger Electron Spectroscopy (AES).

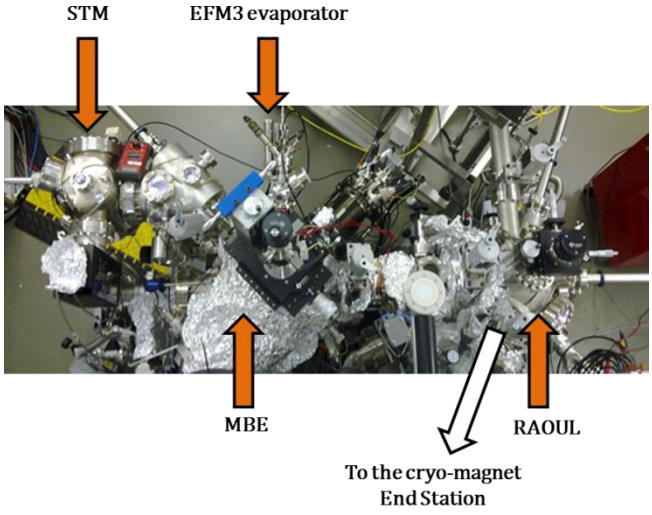

Fig. 2.15: Top view of the DEIMOS UHV system which allows the *in situ* preparation of the samples.

In Our experiments (see section 3.4) a EFM3 Omicron evaporator was assembled in the MBE chamber for the evaporation of the cobalt while our home-made molecules sublimation system was installed in the RAOUL chamber.

2.7 Low Energy Ion Scattering (LEIS)

The Low Energy Ion Scattering (LEIS), also called Ion Scattering Spectroscopy (ISS) is one of the most powerful techniques in the study of the chemical composition of the most superficial layer of surfaces [23]. Due to its ultimate surface sensitivity, it requires ultra high vacuum condition. In the LEIS experiment the sample surface is bombarded with noble gas ions which are accelerated to energy of 500-10000 eV. The ions collide against the atoms forming the outer layer of the surface. The collision can be describe, in first

approximation, as an elastic binary collision of a projectile of mass M_i with energy E_0 with a target of mass M_t at rest; as schematized in fig. 2.16.

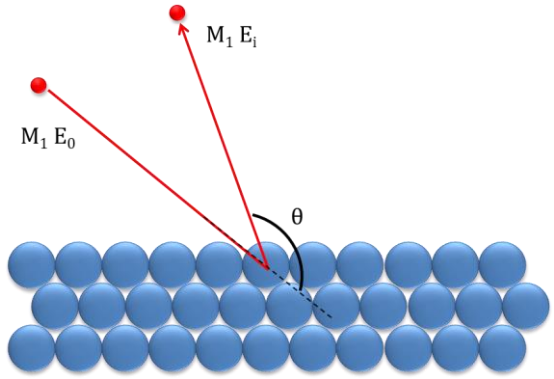

Fig. 2.16: Schematic representation of the elastic binary collision. The projectile collides against the target and it is then back scattered.

In the collision part of the E_0 energy of the projectile is transferred to the target atom. The energy transferred to the target depends on the θ angle and on the mass of the two atoms i.e. M_i and M_t. The projectile is then back scattered with energy E_i and it can be collect by an analyser. An energy scan of the projectiles coming from the target allows to get information on the chemical composition of the outer layer. By knowing the scattering angle (see fig. 2.16) and the mass of the projectile the following equation can be used to calculate the mass of the target atom [24]:

$$E_i/E_0 = \{\pm[(M_t^2 - M_1^2 sin^2\theta)^{1/2} + M_i cos\theta]/(M_1 + M_t)\}^2 \qquad (2.26)$$

However, if the target possesses a low atomic weight the interaction of the projectiles with the surface can modify the structure of the surface [25]. In order to avoid such phenomenon, low energy of the projectile is commonly used ($E_0 < 1000$ eV).

We have used this technique for the study of the cobalt growth on a Cu(100) single crystal. The two elements have high atomic weights and hence small penetration depth of the He^+ ion is expected.

2.8 Scanning Probe Microscopy (SPM)

Scanning probe microscopies (SPM) are one of the most powerful techniques for surfaces studies. In fact, by using a tip as local probe, they allow to achieve local surface information with high spatial resolution down to the atomic scale. Scanning tunneling microscopy (STM) and atomic force microscopy (AFM) are two SPM techniques which are based on quantum mechanical tunneling effect and tip-surface interaction forces, respectively, that made them useful tools for different surface analysis requirement.

2.8.1 Scanning Tunneling Microscopy (STM)

A schematic view of the STM is reported in fig. 2.17 showing the metallic tip, acting as local probe, the conductive sample, the piezo motor system and the feedback circuit. A bias is applied between the tip and the sample surface, hence the tip is brought close to the surface until a quantum mechanical tunneling current (I) flow through a vacuum gap 5-15Å wide. In order to record the STM image the tip is moved across the surface employing the piezo motor system which allows a fine control of the position (X, Y and Z) respect to the sample surface. The use of a feedback loop circuit on the piezos makes possible to scan the surface with a constant tunneling current (constant current mode). The feedback circuit receives the tunneling current variation from the preamplifier and acts on the Z piezo in order to keep the current constant. The STM image information is related to the ΔZ movements of the tip.

In contrast, in height constant mode the feedback circuit is set off during the scan and the STM image information is the tunneling current variation. Working in constant current, i.e. with the feedback loop on, allows the imaging of rough surfaces reducing the probability of tip crashing; however the feedback circuitry time delay imposes a low scanning speed. This limitation can be overcome employing the Z constant mode but the presence of the feedback off imposes strictly

requirements for atomically flat surface in order to prevent tip crashing. All of the images presented in this work were acquired in constant current mode.

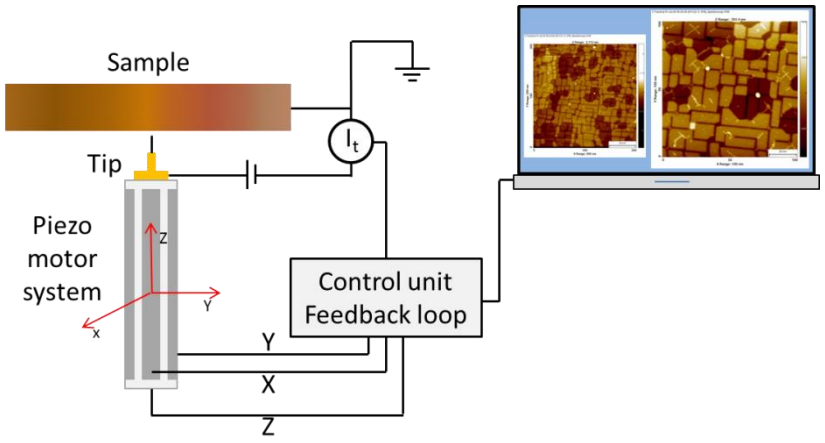

Fig. 2.17: STM scheme. The sample is grounded and the potential is applied to the tip. The feedback loop receives the current from the preamplifier and acts on the piezo motor (in constant current mode). The data are recorded by a computer.

2.8.2 Tunneling effect

In order to better understand the physics that describes the tunneling current involved in the STM experiment a brief description of the quantum mechanical tunneling process is needed. In fig. 2.18 is reported a scheme of a quantum mechanical particle that goes through a finite potential barrier, with V_0 height and d thickness.

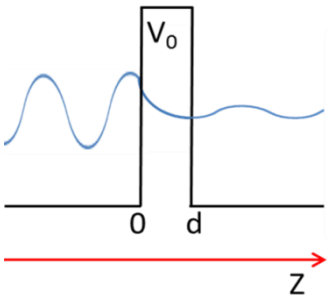

Fig. 2.18: Scheme of the tunnelling barrier. The electron comes from the right part of the barrier.

In the classical view one particle with energy $E < V_0$ cannot overcome the barrier. Using the quantum mechanical approach the electron can be described by a wave function $\psi(z)$ and the probability to overcome the barrier is non-zero. It can be calculated resolving the time independent Schrödinger equation below:

$$\left[-\frac{\hbar^2}{2m}\frac{d^2}{dz^2} + V(z)\right]\psi(z) = E\psi(z) \qquad (2.27)$$

where:

$V(z) = 0$; outside the barrier
$V(z) = V_0$; inside the barrier

The solutions of the equation are in form of planning waves:

$$\psi(z) = \psi(0)e^{\pm kz} \qquad (2.28); \text{ outside the barrier}$$

Where the vector wave k is:

$$k = \sqrt{\frac{2mE}{\hbar^2}} \qquad (2.29)$$

and an exponential decay function inside the barrier for an electron going to the positive Z direction:

$$\psi(z) = \psi(0)e^{-kz} \qquad (2.30)$$

Where the k exponential decay factor is:

$$k = \sqrt[2]{\frac{2m(V_0 - E)}{\hbar^2}} \qquad E < V_0 \qquad (2.31)$$

The probability to find the electron inside the barrier is equal to: $|\psi^2(0)|e^{-2kz}$ and since the thickness d of the barrier is not infinite there is a non-zero probability for the electron to overcome the

barrier. Just considering this simplified tunneling model is possible to highlight the exponential dependence of the tunneling probability to the gap distance d as it occurs for the tunneling current in the STM tip–sample gap.

A more accurate description of the phenomenon was developed starting from the Bardeen formalism [26], which considers the tunneling process related to many independent scattering events that lead the electrons to overcome the tip–sample gap. In this view the electrons tunnel from the states of the tip to ones of the sample or *vice versa*. The problem can be described by the time–dependent Schrödinger equation using time–dependent perturbation theory and assuming that the two systems (tip and sample) are weakly interacting. Hence, considering low bias and applying the Fermi's golden rule for the transition probability, the current can be writes as:

$$I = \frac{2\pi e}{\hbar}\sum_{\mu,\nu}\{f(E_{\mathrm{T},\mu})[1-f(E_{\mathrm{S,v}}+\mathrm{eV})]-f(E_{\mathrm{S,v}}+\mathrm{eV})[1-f(E_{\mathrm{T},\mu})]\}\cdot|M_{\mu,\mathrm{v}}|\cdot {}^{2}\delta(E_{\mathrm{T},\mu}-E_{\mathrm{S,v}}) \qquad (2.32)$$

Where $f(E)$ is the Fermi–Dirac distribution function and $E_{\mathrm{T},\mu}$ and $E_{\mathrm{S,v}}$ are the energy eigenvalue of the state ψ_{μ} of the tip and ψ_{v} of the sample respectively. The $\delta(E_{\mathrm{T},\mu}-E_{\mathrm{S,v}})$ term accounts for the energy conservation of the electron as expected for the elastic tunneling. The $M_{\mu,\mathrm{v}}$ is the tunneling matrix defined as:

$$M_{\mu,\mathrm{v}} = -\frac{\hbar^2}{2m_e}\int\left[(\psi_{\mu})^*\vec{\nabla}\psi_{\mathrm{v}} - \psi_{\mathrm{v}}\vec{\nabla}(\psi_{\mu})^*\right]d\vec{s} \qquad (2.33)$$

In order to calculate the tunnelling matrix the knowledge of the explicit form of the state function of the tip and the sample is needed. However the description of the atomic structure of the two electrodes is not trivial. In detail, the atomic structure of the tip is unpredictable because there is no reproducible preparation at atomic level for it; moreover the tip structure can undergo changes during the STM experiment.

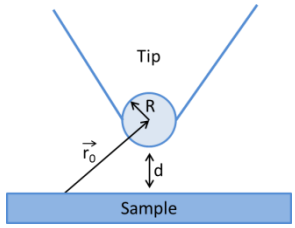

Fig 2.19: Tersoff and Hamann simplify tip scheme view.

To overcome these issues Tersoff and Hamann [27,28] assumed a simplified view of the tip schematizing its apex as reported in fig. 2.19. The exponential decay of the tunnelling current, in respect to the distance, leads to consider that the electron tunnelling process involves mainly the last atom of the tip. Therefore it is possible to assume that the tip apex is spherical. By considering also only the s–waves involved in the process and room temperature or below it gives:

$$I \propto V \cdot \rho_T(E_F) \cdot \rho_S(E_F, \vec{r}_0) \cdot e^{2kR} \qquad (2.34)$$

Where V is the bias, $\rho_T(E_F)$ is the density states of the tip, $\rho_S(E_F, \vec{r}_0)$ is the local density of the state (LDOS) of the sample surface evaluated at the Fermi energy and k is defined as: $k = \frac{\sqrt[2]{(2m_e\phi)}}{\hbar}$; ϕ is the effective barrier height. Under the Tersoff and Hamann assumptions the tip results simply as local probe and the sample contribution to the current is related to its LDOS given by:

$$\rho_S(E_F, \vec{r}_0) = \sum_v |\psi_v(\vec{r_0})|^2 \, \delta(E_v - E_F) \qquad (2.35)$$

Where the exponentially decay of the wave functions $|\psi_v(\vec{r_0})|^2$ on increasing $|\vec{r_0}|$ explains the current dependence to the tip–sample distance. From the last two equations **2.34** and **2.35** it results also that working in current constant mode the final image is the constant LDOS surface of the sample. In fact STM experiments access directly the LDOS of the sample and not its morphology. Obviously the LDOS is related to the morphology but in some cases the STM image is not

corresponding to it. For example imaging Cu_2N islands on Cu surface, by using constant current mode and small bias, the islands are showed as depression instead as protrusion (fig. 2.20). A full monolayer of Cu_2N grown on Cu(100) will be used as substrate for the deposition of the Fe_4Ph molecule in sections 4.6 and 4.7 .

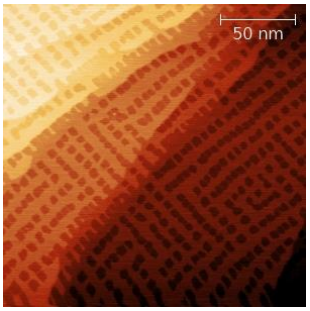

Fig. 2.20: STM image of small island of Cu_2N grown on Cu(100) surface (200pA;2V;200x200nm^2).

2.8.3 Scanning Tunnelling Spectroscopy (STS)

It has been demonstrated that the STM technique is sensitive to the local density of states. This allows to get information on the LDOS with atomic precision. In order to achieve information on the energy dependence of the LDOS the scanning tunnelling spectroscopy can be employed. In this measure the tip is positioned on top the interesting point and the feedback loop is then turned off. A ramp of potential is applied on the tunnelling junction while measuring the tunnelling current. In this way a single point scanning tunnelling spectroscopy is recorded. The data obtained will be the convolution of the LDOS of the tip and the sample. Assuming a flat LDOS for the tip the current is described as:

$$I \propto LDOS_{sample} V \qquad (2.36)$$

Thus the d(I)/d(V) curves provide direct information of the LDOS of the sample. In order to be able to measure the d(I)/d(V) a lock-in detection of an alternate bias is employed. The alternate bias is superimposed to the potential ramp and the lock-in allows to discard the capacitive current. In this way it is possible to record the d(I)/d(V) spectra directly. Generally a further normalization of the data is employed in order to take in account the variation of the transmission coefficient respect to the applied bias [29]. This dependence can be eliminated by using the (d(I)/d(V))/(I/V) as proposed by Stroscio and Feenstra [30,31].

It's important to note that the STS experiment allows a direct measure of the conductance of the investigated point. This is crucial point for the study of inelastic tunnelling process (see chapter 4.7).

2.9 Multiplatform Ultra-High Vacuum (UHV)system

In this work mostly of the surface characterisations were carried out exploiting the multiplatform UHV system at the Center for Scanning Probe Characterisation Techniques (CeTeCS) of the Dept. of Chemistry at Florence University (fig. 2.21). The system offers the possibility to prepare the samples and their investigation *in situ* employing XPS, UPS, LEIS and STM techniques for the characterisation.

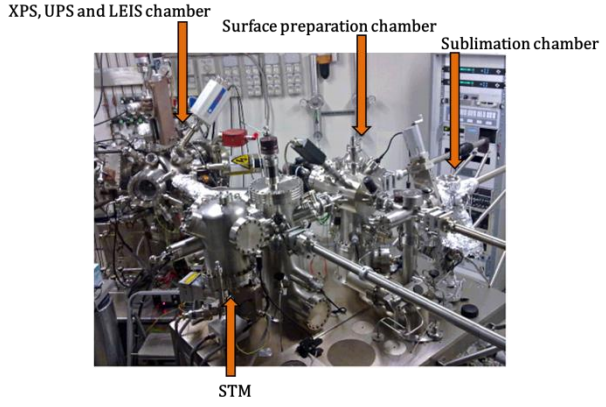

Fig 2.21: Picture of the multiplatform UHV system which offers the possibility to employ XPS, UPS, LEIS and STM characterisation techniques.

2.9.1 Sublimation chamber

The sublimation chamber was equipped with the system for the molecular sublimation described in section 2.2 and with a Sycom quartz crystal microbalance. The base pressure of the chamber was 10^{-10} mbar.

2.9.2 XPS, UPS and LEIS chamber

The chamber was equipped with a SPECS Microfocus 600 monochromatic source (Al K_α radiation), coupled with a helium discharge lamp and with a hemispherical electron/ion energy analyser (VSW mounting a 16-channel detector). The sample was mounted on a manipulator which permitted the variation of the angle θ between the normal to the sample and the analyser while maintaining the angle between the analyser axis and the x-ray and ultraviolet sourcesfixed at 54.5°. The XPS source was operated at a power of 100 W (10 kV and 10 mA). To record LEIS spectra we used a focused (approximately 1-2 mm^2) beam of ions generated by a Omicron ISE 100 Gun with an energy range 600 eV to 1500 eV impinging on the surface at an angle of 45° using He^+ as primary ion sources. The scattering angle was 135°, and the kinetic energy of the scattered ions was measured by using the same hemispherical analyser employed for XPS.

2.9.3 STM Omicron system

In the STM chamber is housed an Omicron Variable temperature STM which can operate in 25-1500 K range. We exploited the low temperature range for the hybrid surface investigation using electrochemically etched tungsten tip. The potential was applied to the tip while the sample is grounded. The base pressure of this chamber was $5 \cdot 10^{-11}$mbar.

References

[1] A. Barone and G. Paternò, *Physics and application of the Josephson effect,*Wiley-Interscience (1982).

[2] Bukel, *Superconductivity: Fundamentals and Application*, VCH, Weinheim (1991).

[3] J. Clark and A. I. Braginski, *The SQUID Handbook*, Wiley-VCH (2004).

[4] H. B. G. Casimir and F. K. du Pré, Physica **5**, 507 (1938).

[5] K. S. Cole and R. H. Cole, J. Chem. Phys. **9**, 341 (1941).

[6] S. Voss, M. Fonin, L. Burova, M. Burgert, Y. S. Dedkov, A. B. Preobrajenski, E. Goering, U. Groth, A. R. Kaul, and U. Ruediger, Appl. Phys. A **94**, 491 (2008).

[7] M. Mannini, P. Sainctavit, R. Sessoli, C. Cartier dit Moulin, F. Pineider, M.-A. Arrio, A. Cornia, and D. Gatteschi, Chem. Eur. J. **14**, 7530 (2008).

[8] L. Margheriti, D. Chiappe, M. Mannini, P.-E. Car, P. Sainctavit, M.-A. Arrio, F. B. de Mongeot, J. C. Cezar, F. M. Piras, A. Magnani, E. Otero, A. Caneschi, and R. Sessoli, Adv. Mater. **22**, 5488 (2010).

[9] L. Margheriti, M. Mannini, L. Sorace, L. Gorini, D. Gatteschi, A. Caneschi, D. Chiappe, R. Moroni, F. B. de Mongeot, A. Cornia, F. M. Piras, A. Magnani, and R. Sessoli, Small **5**, 1460 (2009).

[10] A. Einstein, Ann. Phys. **17**, 132 (1905).

[11] J. J. Yeh and I. Lindau, At. Data Nucl. Data Tables **32**, 1 (1985).

[12] J. J. Yeh, *Atomic Calculation of Photoionization Cross-Sections and Asymmetry Parameters*, Gordon Breach Sci. Publ. (1993).

[13] H. Wende, Rep. Prog. Phys. **67**, 2105 (2004).

[14] A. Cornia, M. Mannini, P. Sainctavit, and R. Sessoli, Chem. Soc. Rev. **40**, 3076 (2011).

[15] J. Stohr and H. C. Siegmann,*Magnetism - From Fundamentals to Nanoscale Dynamics*, Springer (2006).

[16] H. A. Z. Kramers, Phys. **39**, 826 (1926).

[17] P. A. M. Dirac, Proc. Roy Soc. **A123**, 714 (1929).

[18] B. Thole, P. Carra, F. Sette, and G. van der Laan, Phys. Rev. Lett. **68**, 1943 (1992).
[19] P. Carra and M. Altarelli, Phys. Rev. Lett. **70**, 694 (1993).
[20] C. Chen, Y. Idzerda, H.-J. Lin, N. Smith, G. Meigs, E. Chaban, G. Ho, E. Pellegrin, and F. Sette, Phys. Rev. Lett. **75**, 152 (1995).
[21] R. Wu and A. J. Freeman, Phys. Rev. Lett **73**, 1994 (1994).
[22] J. Stöhr, J. Electron Spectros. Relat. Phenomena **75**, 253 (1995).
[23] H. Brongersma, M. Draxler, M. Deridder, and P. Bauer, Surf. Sci. Rep. **62**, 63 (2007).
[24] H. Niehus and R. Spitzl, Surf. Interface Anal. **17**, 287 (1991).
[25] H. H. Brongersma, M. Carrere-Fontaine, R. Cortenraad, a. W. Denier van der Gon, P. J. Scanlon, I. Spolveri, B. Cortigiani, U. Bardi, E. Taglauer, S. Reiter, S. Labich, P. Bertrand, L. Houssiau, S. Speller, S. Parascandola, H. Ünlü-Lachnitt, and W. Heiland, Nucl. Instruments Methods Phys. Res. Sect. B Beam Interact. with Mater. Atoms **142**, 377 (1998).
[26] J. Bardeen, Phys. Rev. Lett. **6**, 57 (1961).
[27] J. Tersoff and D. R. Hamann, Phys. Rev. Lett. **50**, 1998 (1983).
[28] J. Tersoff and D. R. Hamann, Phys. Rev. B **31**, 805 (1985).
[29] A. Selloni, P. Carnevali, E. Tosatti, and C. Chen, Phys. Rev. B **31**, 2602 (1985).
[30] J. Stroscio, R. Feenstra, and A. Fein, Phys. Rev. Lett. **57**, 2579 (1986).
[31] R. Feenstra and P. Mårtensson, Phys. Rev. Lett. **61**, 447 (1988).